Orientation dynamics of nonspherical particles under surface gravity waves

Michelle H. DiBenedetto,[*] Jeffrey R. Koseff, and Nicholas T. Ouellette

Bob and Norma Street Environmental Fluid Mechanics Laboratory, Department of Civil and Environmental Engineering, Stanford University, Stanford, California 94305, USA

Experiments were conducted with three-dimensional printed disks and rods to study the orientation dynamics of nonspherical particles under surface gravity waves. Trials were run with both neutrally buoyant and slightly negatively buoyant particles, which were large enough that inertia due to their finite size was important. Although the particles had a broad distribution of initial orientations, over time the waves were observed to focus these orientations toward a preferred angle that agreed with theory. Negatively buoyant particles additionally exhibited a tendency to adopt an orientation that maximized vertical drag. The overall orientation can be described as the result of a competition between the orientation favored by waves and the orientation favored by settling. The spread about the mean orientation was also observed to increase with wave strength. Finally, the stabilization of out-of-plane orientations of disk-shaped particles was observed due to their finite size.

I. INTRODUCTION

Many natural and industrial flows contain transported particles that are not spherical. The shape and rotation of nonspherical particles can complicate the prediction of their dynamics and have been an active topic of recent study. However, much of this work has focused on particles in the two limits of microscale Stokes flows [1–3] or isotropic turbulence [4], despite the wide range of relevant situations between these cases. In particular, there has been little investigation of the dynamics of nonspherical particles in flows driven by surface gravity waves. Waves are a dominant characteristic of flows near the ocean surface, in estuaries, and along coastlines. Such environmental flows routinely carry microplastics, algae, sediment, ice, and small organisms, all of which are small particles that are generically nonspherical. Understanding how waves influence and control the orientation of these particles is a key question, since the particle orientation determines the lift and drag forces on the particle. These forces in turn control the settling velocity, an essential parameter for modeling their transport and position in the water column. Additionally, for active particles such as zooplankton, the effects of the flow on orientation can control their ability to navigate and explore their environment [5].

Although some research has been done on pointlike, noninertial spheroids under waves, the results are not yet fully in agreement. Motivated by understanding the rheology of grease ice, a theoretical study of small noninertial disks moving under linear deep-water surface gravity waves argued that the particles will align with the strain field of the waves and tumble at the wave frequency [6]. More recently, we argued instead that noninertial point particles will adopt a preferred orientation with an oscillation at the wave frequency, not a tumble; we proved this analytically [7] for any linear gravity waves and showed that the effect remains when small particle inertia is included in a numerical study [8]. All of this work, however, treated the particles as pointlike and neglected

---

*mdiben@stanford.edu

any effects of flow inertia around the particle. But many particles of interest in the ocean fall within an intermediate size regime where the effects of finite size and inertia become relevant. In particular, microplastics—that is, plastic particles that are defined to be up to 5 mm in length scale—are large enough that the point particle approximation may not be fully valid.

When finite particle mass is included, the particles will also tend to sediment. The settling velocity of a particle controls its time in the water column, directly influencing its transport and dispersion. The effects of inertia on sedimenting spherical particles has been studied [9], as well as the interaction between particle inertia and turbulence [10,11]. Less is known, however, about settling nonspherical inertial particles. It has been argued that they should adopt a preferred settling orientation that is a function of shape and Reynolds number; but turbulence can diffuse the particle orientation about this preferred value [12]. This diffusive effect is also a function of the particle shape and the turbulence [13]. These results suggest the possibility of competition between the tendency of the settling of a particle to set a preferred orientation and the tendency of the turbulence to scramble the orientation. Given that we have shown that waves can also set a preferred orientation [7,8], the orientational behavior of settling nonspherical inertial particles in wavy flows is very difficult to predict.

In this paper we present experimental results on the orientation of such particles under surface gravity waves. We consider both negatively buoyant (i.e., settling) and nearly neutrally buoyant (but still finite-sized) particles. When particles are introduced into the flow with a distribution of orientations, we confirm that the waves can over time focus this distribution toward the preferred orientation we previously found theoretically [7,8]. As this orientation is not the same as what would be set by settling alone, we thus show that even without turbulence, waves are sufficient to scramble the orientations of settling particles. However, we also find evidence for competition between the effects of settling and waves. Finally, we also find that inertia due to finite particle size stabilizes the out-of-plane orientation in waves, even though it is unstable for noninertial point particles.

We begin below by further discussing the context of our work in Sec. II. We then describe our experimental methods in Sec. III, including the wave facility, the measurement technique, and the fabrication of our particles. Our results are discussed in Sec. IV. Finally, we summarize and discuss our findings in Sec. V.

II. BACKGROUND

Although the orientation dynamics of infinitesimal, noninertial particles is completely described by Jeffery's equation [14], less is known analytically for particles that have inertia relative to the flow. Such inertia can be due to both size and density. Most of the work on nonspherical inertial particles has considered the effects of density [15–17], since that is easier to introduce as a small parameter. There are still many open questions, however, about particles that are inertial due to their finite size [4,18,19].

Finite-size inertia has typically been studied in turbulent flows via laboratory experiments, as it is difficult to capture faithfully in numerical models. Some experiments have been conducted with large, near neutrally buoyant particles in homogenous isotropic turbulence to assess the effects of finite size on rotation statistics [20,21]. In these isotropic flows, the orientation statistics of the particles remain isotropic as well. Settling experiments have been conducted of finite-sized, nonspherical particles, but mainly in quiescent flows [22–25] or turbulence [26,27]. Particle inertia has also been experimentally investigated with fibers in turbulence, and it was shown that it can have a non-negligible effect on particle rotation statistics [28]. Therefore, this experiment expands on the current body of research by analyzing the orientation of inertial nonspherical particles in an anisotropic, unsteady flow.

For small, noninertial spheroids in flows driven by surface gravity waves, we previously found that particles tend to a set of stable orientations. Using both theoretical analysis and numerical simulations, we showed that particles settle onto a stable oscillation in the plane of the waves about a preferred orientation that is only a function of the shape of the particle [7,8]. Going forward, we
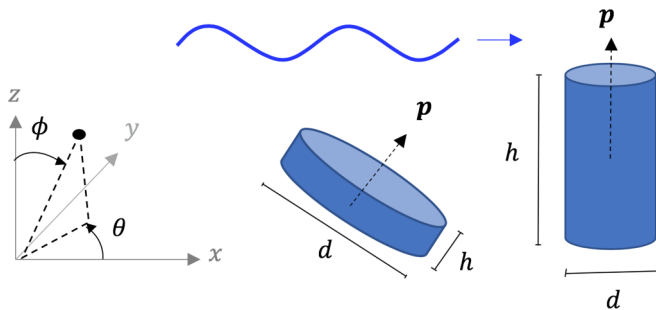
FIG. 1. Coordinate system and geometry of the 3D-printed particles. Elongated and flattened cylinders were used to approximate rods and disks, respectively. Their orientation is described by a unit vector p directed along the symmetry axis. The azimuthal angle θ captures the orientation of the particles out of the plane of the wave motion, and the polar angle ϕ is the angle measured from the vertical (z) axis.

will call this orientation the wave-preferred orientation. For settling (that is, negatively buoyant) nonspherical particles in quiescent flow, studies have shown that settling particles with intermediate particle Reynolds numbers in the range $5.5 < \mathrm{Re}_p < 200$ adopt stable orientations that maximize their drag [25,29]. In this case, maximizing drag corresponds to the particles horizontally aligning their longest length scale. We will call this orientation the settling-preferred orientation.

We describe the particle's orientation by a unit vector p pointing along its axis of symmetry, as shown in Fig. 1. For both the wave-dominated case and the settling-dominated case, the polar angle ϕ is sufficient to characterize the preferred orientation; we denote the wave-preferred angle as ϕ_w^* and the settling-preferred angle as ϕ_s^*. Settling disks (that is, oblate particles) have $\phi_s^* = 0$, and settling rods (that is, prolate particles) have $\phi_s^* = \pi/2$. These orientations correspond to maximized vertical particle drag, which agrees with theory [30] and preliminary experiments conducted with the particles falling in quiescent flow. Theoretically, the azimuthal angle θ_s^* can take any value in these cases.

In the limit of vanishing particle inertia, the wave-preferred angle is only a function of shape and is given by $\tan \phi_w^* = \Gamma$ where Γ is the particle aspect ratio [7,8]. Assuming that the waves lie in the x-z plane as shown in Fig. 1, $\theta_w^* = 0$. This orientation is solely a function of the particle's shape, but the waves also drive an oscillation about this orientation with an amplitude that is both a function of the particle's shape and the wave characteristics [7].

Finally, in both waves and steady shear flows, the log-rolling mode (that is, where the particle's axis of symmetry is perpendicular to the shear plane) is expected to be unstable for noninertial particles. However, theoretical [16,31] and numerical [32,33] work has suggested that both weak particle and fluid inertia can in fact stabilize this mode for oblate particles.

III. METHODS

A. Flow facility

Laboratory experiments were conducted in the Bob and Norma Street Environmental Fluid Mechanics Laboratory at Stanford University. The experimental setup consisted of an enclosed rectangular tank measuring 488 cm long, 60 cm deep, and 30 cm wide. A vertically oscillating triangular wavemaker was positioned at one end of the tank; the opposite end had a horse-hair beach to dissipate energy and prevent wave reflections from the back wall. A schematic of the experiment is shown in Fig. 2. The tank was filled with deionized water, and the density was then adjusted using salt and measured using an Anton-Paar density meter (model DMA4500).

The right-angled wavemaker plunger was 40 cm tall, 30 cm wide, and 25 cm long so that its aspect ratio was 1.6, which falls within the parameter range investigated for wave making in
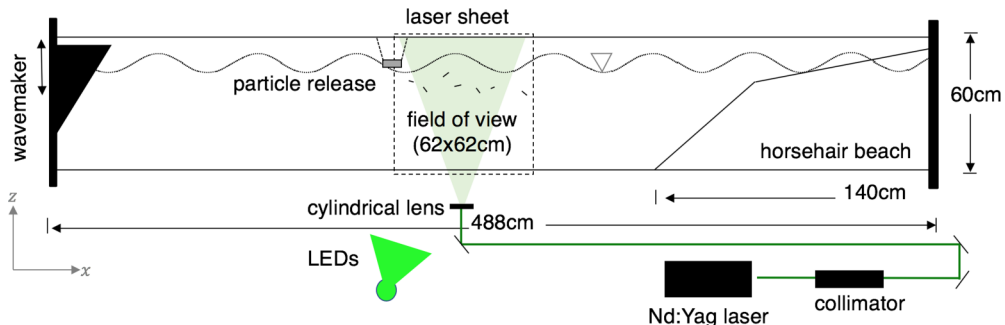
FIG. 2. Schematic (not to scale) of the experimental setup. Waves are generated on the left side of the tank by a plunging wave maker and are dissipated on the right side by the horse-hair beach. A laser is directed upward through the bottom of the tank to illuminate tracer particles. Bright LEDs provide illumination for the nonspherical particles through the side of the tank. The horse-hair beach is arranged to maximize the amount of horsehair at the top of the water column where the waves are strongest but minimize its lateral extent into the tank.

Ref. [34]. A train of progressive waves could be generated with varying amplitudes and wavelengths by changing the wavemaker stroke amplitude and frequency. The wave amplitude was measured using a wave gauge downstream of the field of view.

B. Particles

To allow maximal control over the shape and size of the nonspherical particles, the particles were manufactured by Sculpteo and Protolabs using Selective-Laser-Sintering three-dimensional (SLS 3D) printing. This 3D printing technique was used because of its sub-millimeter accuracy and compatibility with nylon 12, which has a specific gravity (SG) of 1.01 and thus allows us to manufacture particles denser than fresh water. This SG allowed us to conduct experiments with either negatively and neutrally buoyant particles easily by manipulating the density of the water in the wave tank using NaCl; we denote the ratio of the particle density ρ_p to the fluid density ρ by β. However, the density of the printed particles was not always identical and equal to that of the source material due to the manufacturing process, and so we measured the particle density after printing to ensure accurate experimental conditions. To measure the particle densities, we placed the particles in a standard solution of specific gravity 1.01. The solution density was then was altered until most of the particles were neutrally buoyant and therefore in suspension. The precision (captured by the error bars reported in Table I) is reported as the range between the density where all of the particles were negatively buoyant to the density where none of them were.

Nylon is also a convenient material choice because it absorbs very little water. The equilibrium water absorption for nylon 12 is only 1%, so the particle size varied negligibly when soaked in water (unlike, say, particles made of hydrogel). Nevertheless, we stored the particles in water when not in

TABLE I. Particle sizes and shapes, settling velocities, and particle Reynolds numbers. 95% confidence intervals are reported for the particle length scales and settling velocities.

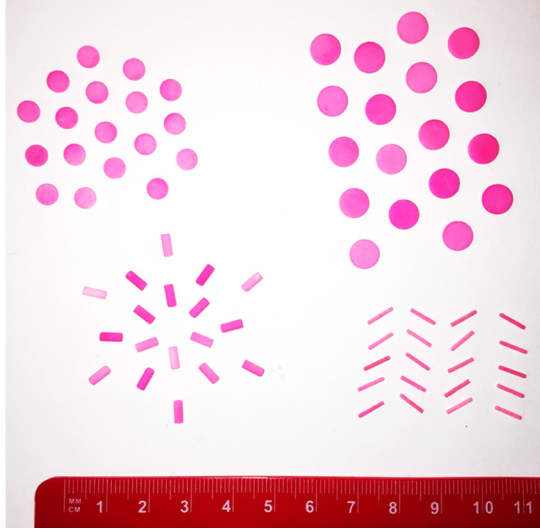| Particle	Γ	h (mm)	d (mm)	w_s (cm/s)	ρ_p (kg/m^3)	Re$_p$
Large disk	0.16	1.15 ± 0.01	7.0 ± 0.01	0.93 ± 0.002	1.005 ± 0.001	66
Small disk	0.22	1.1 ± 0.01	5.0 ± 0.01	0.91 ± 0.002	1.005 ± 0.001	46
Short rod	4.1	6.2 ± 0.01	1.5 ± 0.01	0.70 ± 0.002	1.005 ± 0.001	46
Long rod	7.8	6.75 ± 0.04	0.86 ± 0.02	0.90 ± 0.006	1.01 ± 0.002	60

FIG. 3. Photo of the particles used in the experiments after having been dyed with Rhodamine. Clockwise from the top left are small disks, large disks, long rods, and short rods. The ruler provides a scale in centimeters.

use to ensure that they maintained their maximum water absorption. Finally, to make the particles easier to illuminate, we cooked them in a solution of Rhodamine 6G to make them fluorescent [35].

A set of 20–25 particles was printed in each of four different shapes, which we label long rods (aspect ratio $\Gamma = 7.8$), short rods ($\Gamma = 4.1$), small disks ($\Gamma = 0.22$), and large disks ($\Gamma = 0.16$). The aspect ratio Γ was defined to be the ratio of the length of the particle along its axis of symmetry to the length of the particle along the perpendicular axis. The (measured) properties of the particles are shown in Table I. The lengths reported in Table I are averages of all the manufactured particles; the 95% confidence interval for all of the particles was on the order of 0.01 mm. A sample image of the particles used in the experiment is shown in Fig. 3.

Particle settling velocities w_s were measured by letting the particles fall in quiescent fresh water in the same tank in which the experiments were conducted. The particle Reynolds number $\mathrm{Re}_p = l w_s / \nu$ is based on w_s, their largest length scale l, and the kinematic viscosity of water ν. In fresh water, all of the particles have transitional Reynolds numbers; thus, Stokes-flow approximations do not necessarily hold for calculating the forces on the particles.

The particles were released into the wave field from a small suspended swing. Particles were placed on the swing, which sat above the quiescent water level in the center of the tank. When the waves were initiated, the particles were pushed off the swing by the passing waves. After the particles were released, the swing was lifted out of the water. This process allowed a repeatable particle release with minimal disturbance to the flow.

C. Image processing and data analysis

Both the flow velocity and the printed particle velocities were measured using optical particle tracking. To measure the flow, we used small (45–53 μm diameter), neutrally buoyant fluorescent orange polyethylene microspheres purchased from Cospheric. These particles were small enough that they accurately follow the flow in our experiments [with Stokes numbers of St $\sim O(10^{-6})$]. The tracers were illuminated by a vertical laser sheet made using a cylindrical lens and an Nd:YAG laser (frequency-doubled to operate at 532 nm) positioned below the tank, while the 3D-printed particles were illuminated with high-power green (530 nm) LEDs. Particles were imaged with a Photron FASTCAM SA5 CMOS camera at 60 or 125 frames per second (depending on the flow speed)

TABLE II. Wave cases and nondimensional parameters, including the wave frequency ω, amplitude A, wave number k, wave steepness kA, relative depth kH, and reflection coefficient R_w.

Wave case	ω (rad/sec)	A (cm)	k (1/m)	kA	kH	R_w
WC2	2π	3.5	4.3	0.15	1.8	0.03
WC3	3π	3.3	8.8	0.29	3.7	0.02
WC4	4π	2.3	14.1	0.32	5.8	0.01

with a resolution of 1024×1024 pixels. The camera was equipped with a Sigma 30 mm f/1.4 EX DC HSM lens and an orange bandpass filter (560–600 nm).

Image processing was more challenging than in many cases due to the surface gravity waves, which focus light from both the laser sheet and the LEDs in a time-varying manner. To lessen this effect, separate background images were created for each wave phase. These background images were computed by taking the median of multiple images (between 10 and 50, depending on the wave frequency and frame rate) at a given wave phase. The images were also calibrated to remove lens distortion using photos of a regular checkerboard pattern. This phase-resolved background-image approach allowed us to accurately track particles below the surface; however, particles at or near the surface could not be tracked due to reflections and shimmering effects. Finally, images were processed to acquire particle tracks and velocities using a predictive tracking algorithm [36,37]. A Gaussian fit to the pixel brightnesses was used for subpixel accuracy for the tracer particles; for the larger nonspherical particles, the particle centroid was used.

We first performed a set of flow characterization experiments to determine the velocity field in the flow using tracer particles. Once we had established that the flow fields were well behaved and consistently produced the same velocity fields, we repeated the experiments with only the large nonspherical particles of interest. We were careful to ensure that the setup was identical so that the mean wave characteristics measured from the tracer particles could be applied to the analysis of the large nontracer particles.

From both theoretical arguments and empirical evidence, we expected the large, nonspherical particles to orient themselves in the plane of the waves [8]. Thus, we assumed that the particles with imaged aspect ratios approaching their physical Γ had their axes of symmetry aligned into the plane of the waves and thus in the plane of the field of view. This assumption allowed us to relate the angle of the particles in the image to the particle's polar angle ϕ, as shown in Fig. 1. Note that due to the symmetries of the problem, we report only values of ϕ between 0 and $\pi/2$.

D. Wave cases and flow characterization

Our flow facility was capable of making small-amplitude deep water waves as well intermediate-depth waves. For all experiments, we maintained a fixed water depth of $H = 41.5$ cm. The wave frequency ω was set by the frequency of the wave plunger, and the wave amplitude A was measured at the surface with a wave gauge. The wave number k was calculated via $\omega^2 = gk \tanh kH$ (where g is the acceleration due to gravity), the dispersion relation for linear surface gravity waves. This calculation was confirmed *a posteriori* from measurements of the velocity gradients.

We consider three wave cases here, which we label by their wave frequency as shown in Table II. Each case had a different frequency and therefore a different relative depth kH. WC2 approaches the shallow water limit ($kH < \pi/2$), WC4 approaches the deep water limit ($kH > 2\pi$), and WC3 is an intermediate-depth case. The wave steepness at the surface is given by the nondimensional parameter kA. WC2 has a low steepness, whereas WC3 and WC4 are both very steep at the surface. For each wave case, data were collected and averaged over an ensemble of three 90 s runs.

We characterized the wave velocity fields using particle-tracking velocimetry, as described above. To construct velocity fields, we interpolated the tracer data onto a 0.3×0.3 cm grid and phase-averaged over the two-dimensional field of view. These measurements were then compared to the

predictions from linear wave theory. Under this assumption, the velocity components for an arbitrary water depth H are given by

$$u(x, z, t) = A\omega \frac{\cosh[k(z + H)]}{\sinh(kH)} \cos(kx - \omega t) \tag{1}$$

and

$$w(x, z, t) = A\omega \frac{\sinh[k(z + H)]}{\sinh(kH)} \sin(kx - \omega t). \tag{2}$$

For these equations, the origin ($z = 0$) lies at the free surface. To compare with theory, the gridded velocity data was fit to a sinusoid in time at each point in space. The mean value and amplitude of the sinusoid were then determined. The wave phase is a function of x and t, but the amplitude of the velocity signals is only a function of z. Thus, the amplitudes of the measured velocities (U, W) were found as a function of depth. We note that due to the closed nature of the tank, a reverse current set up near the bottom to balance the Stokes-drift mass transport at the surface. Thus, the mean horizontal velocities do not vanish. We account for this reverse current by adding a mean drift $\bar{u}$ to the horizontal velocity, so that we have

$$u(x, z, t) = U(z) \cos(kx - \omega t) + \bar{u} \tag{3}$$

and

$$w(x, z, t) = W(z) \sin(kx - \omega t). \tag{4}$$

We plot the measured U and W values versus the predictions from linear wave theory in Figs. 4(a) and 4(b). The agreement is very good, except very near the free surface where the imaging is noisy. Finally, we also note that the horse-hair beach at the end of the tank minimized wave reflections. This was quantified using the approach for colocated horizontal and vertical velocity measurements developed in Ref. [38]. The reflection coefficient R_w reported in Table II is given by A_r/A, the ratio of the reflected wave amplitude to the incident wave amplitude. The small values of R_w for all of our experimental cases indicate that wave reflection is negligible in our facility.

Stokes drift velocities were measured directly from particle tracks. Tracks longer than two wave periods were used to calculate mean displacements. These particle tracks were then binned by depth and averaged over the data records. In Fig. 4(c), these data are plotted and compared to the theoretical prediction for the Stokes drift velocity u_s given by

$$u_s(z) = A^2 \omega k \frac{\cosh[2k(z + H)]}{2 \sinh^2(kH)}. \tag{5}$$

Note that there are non-negligible Stokes drift velocities at the bottom of the tank. These arise due to the wave streaming [39] induced by the interaction of the bottom boundary layer with the waves. The streaming is confined to the bottom 2 cm of the tank and thus can be ignored in our analysis, since we consider only the upper portions of the water column.

Finally, we note that since the wave strength decays with depth in our experiments, we can examine particles at different depths in the water column to expand our range of wave cases studied. To do so, we define a depth-dependent nondimensional wave shear $ka(z)$. First, we can define a depth-dependent shear based on the analytical wave equations (1) and (2). The equations for du/dz and dw/dx are identical oscillations:

$$\frac{du}{dz} = \frac{dw}{dx} = kA\omega \frac{\sinh[k(z + H)]}{\sinh(kH)} \cos(kx - \omega t). \tag{6}$$

Normalizing by the wave frequency ω and removing the oscillation, we have

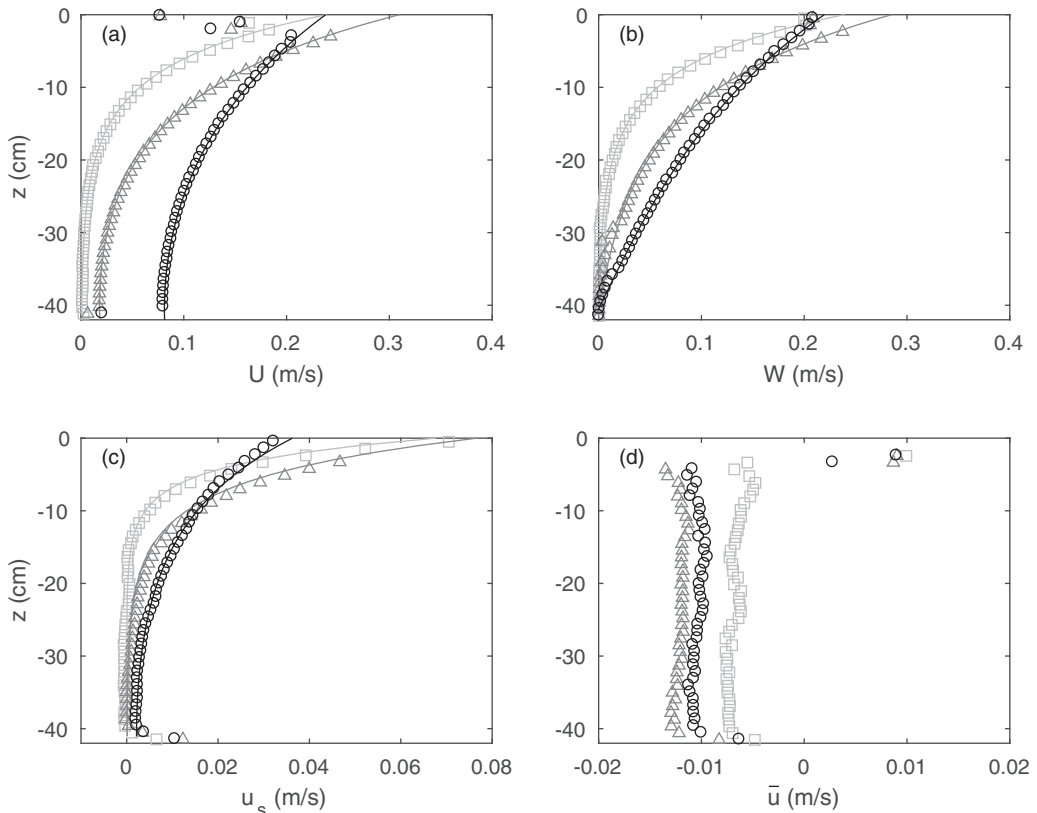$$ka(z) = kA \frac{\sinh[k(z + H)]}{\sinh(kH)}. \tag{7}$$

FIG. 4. Mean flow characteristics. Measured average wave amplitudes (a) U and (b) W as a function of depth for the three wave cases (symbols) are plotted along with the predictions from linear wave theory (solid lines). (c) Measured Stokes drift u_s velocities (symbols) as a function of depth along with the theoretical predictions (solid lines). (d) Measured mean Eulerian flow velocities $\bar{u}$ as a function of depth. For all panels, case WC2 is shown with circles, case WC3 is shown with triangles, and case WC4 is shown with squares.

We can use this to formulate a shear particle Reynolds number, $\mathrm{Re}_s = \gamma l^2 / \nu$ defined by the shear rate γ, the longest length scale of the particle l, and the kinematic viscosity of water ν. In this case, $\gamma = ka(z)\omega$. The value of Re_s represents the effect of fluid inertia on the particle's orientation, while the effect of particle inertia is typically represented with the product $\beta \mathrm{Re}_s$ [17]. In this case, both numbers are approximately equal as $\beta \approx 1$.

IV. RESULTS

Here we describe the measured effects of waves on both negatively buoyant and nearly neutrally buoyant nonspherical particles. Our results are largely consistent with our previous theoretical work on idealized particles [7,8]. We find that particles tend toward a (wave-averaged) preferred orientation, but that this effect is weaker when the particles are also settling. Indeed, we observe a competition between the (differing) wave-driven and settling-driven preferred orientations. We also show that the finite inertia of the particles in this experimental study can stabilize the out-of-plane log-rolling position, even though this position is unstable for noninertial particles, and β is close to 1.
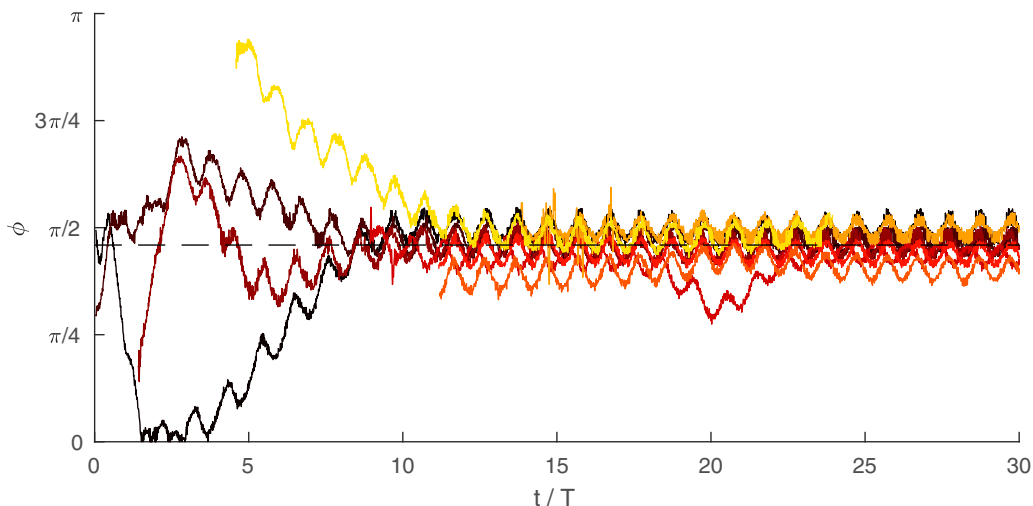
FIG. 5. Time series of the polar angle ϕ for several neutrally buoyant ($\beta = 1$) long rods in WC2 waves. Though their initial ϕ values were uncontrolled, the particles all settle onto an oscillatory limit cycle at the wave frequency about a similar angle. The wave-preferred angle ϕ_w^* expected from theory is marked with a dashed line.

A. Temporal effects of waves: Orientation focusing

As described above, in our previous theoretical and numerical work we found that waves drive nonspherical particles to oscillate about a preferred polar angle ϕ_w^*. Experimentally, we find that this result indeed holds for the finite-sized particles we consider here. An example of this behavior is shown in Fig. 5, where the polar angle ϕ of several neutrally buoyant long rods in wave case WC2 is plotted over time. In each case, ϕ approaches ϕ_w^* with a superimposed oscillation at the wave frequency. Even though each rod had a different initial orientation, they all oscillate about a similar angle after approximately 12 wave periods. The stability of this orientation can also be seen in Fig. 5 by the perturbation away from this preferred orientation around $t/T = 20$ that is quickly damped.

This temporal angular focusing is also apparent statistically. We computed the probability density functions (PDFs) of ϕ for long rods at each instant in time, as shown in Fig. 6. Data in this case were taken only from particles in the top part of the water column, where $ka(z) \geqslant 0.05$, since particles that are lower in the water column may not actually feel the waves. Figure 6(a) shows the evolution of these PDFs with time for neutrally buoyant particles, and the development of a peak in the PDF at ϕ_w^* is clearly visible as time advances. However, there is also a second peak at $\phi = \pi/2$, which in this case is ϕ_s^*, the preferred angle for *settling* rods. This peak is even more prominent for *negatively* buoyant rods, as shown in Fig. 6(b). In both of these cases, we observe bimodal PDFs of ϕ with peaks at both ϕ_w^* and ϕ_s^*, suggesting that there is a competition between waves and settling in determining the orientation of these particles. When settling is stronger than the wave action, the peak at ϕ_s^* is more prominent, and vice versa.

The statistical moments tell a similar story. The mean $\overline{\phi}$ and standard deviation σ_ϕ are shown for neutrally buoyant long rods in Fig. 7 and for negatively buoyant short rods in Fig. 8. These plots show that when the particles are first released into the flow, they have nearly random orientations. As the particles spend more time in the waves, however, the distribution of particle orientations becomes less uniform: the standard deviation of the particle orientations decreases, and the mean tends toward a preferred value close to ϕ_w^*. We also, though, observe some dependence of the timescale over which this orientation focusing occurs on the particular characteristics of the waves, leading us to consider the effects of wave strength below.
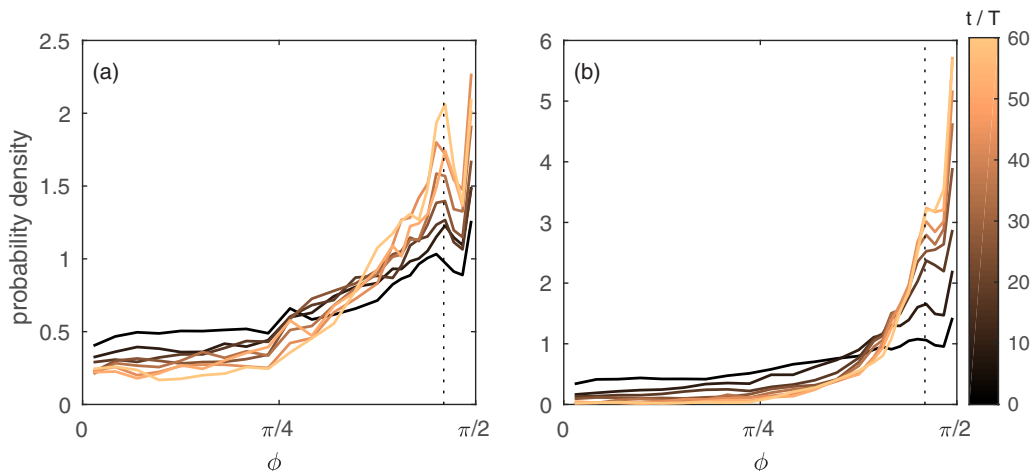
FIG. 6. PDFs of the polar angle ϕ of long rods in waves with (a) $\beta = 1.01$ and (b) $\beta = 1$ at different times, as indicated by the shading. The dotted line shows the theoretical wave-preferred angle ϕ_w^*; the settling-preferred angle is $\phi_s^* = \pi/2$. Data are combined from all three wave cases but only for particles in regions where $ka(z) \geqslant 0.05$.

Thus, our measurements show that nonspherical particles in waves do not randomly sample all angles (as would be expected for tumbling particles), but rather that over time the distributions of their orientations sharpen. However, we observe not unimodal PDFs, as would be expected if a single physical mechanism were setting the preferred alignment, but rather bimodal PDFs, suggesting competing effects—in this case between waves and gravitational settling. This interpretation in turn suggests that by varying the strength of the waves, we ought to see the orientation PDFs change: once the waves are weak enough, settling alone should dominate the particle dynamics. We can test this hypothesis by considering the particles at different depths in the water column, since the nondimensional wave strength $ka(z)$ is a function of depth.
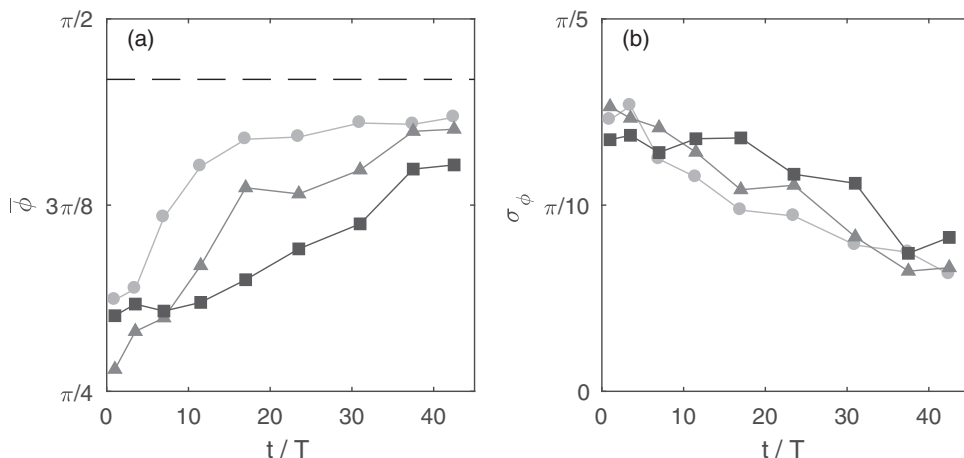

FIG. 7. Evolution of the (a) mean and (b) standard deviation of the polar angle ϕ of neutrally buoyant ($\beta = 1$) long rods in waves as a function time. Data from WC2, WC3, and WC4 are shown by ●, ▲, and ■, respectively. For all cases, data are included only for particles in regions with $ka(z) \geqslant 0.05$.
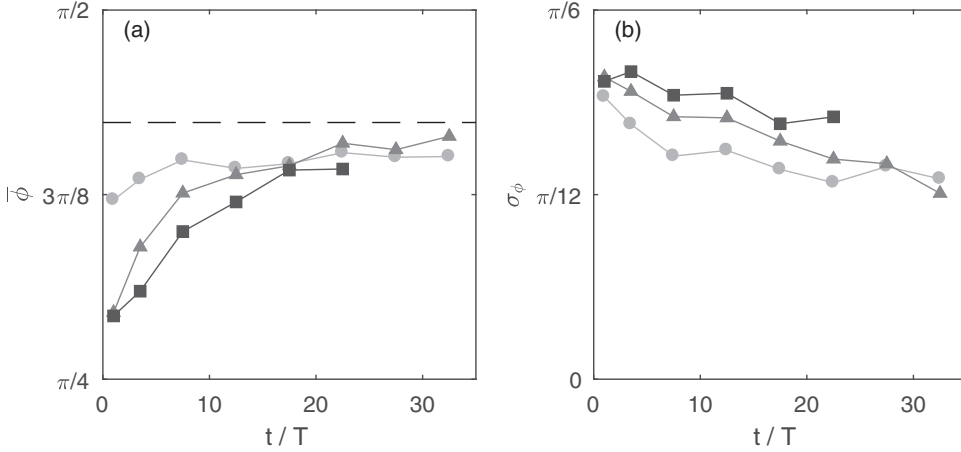
FIG. 8. Evolution of the (a) mean and (b) standard deviation of the polar angle ϕ of negatively buoyant ($\beta = 1.005$) short rods in waves as a function time. Data from WC2, WC3, and WC4 are shown by ●, ▲, and ■, respectively. For all cases, data are included only for particles in regions with $ka(z) \geqslant 0.05$.

B. Effects of wave strength

To isolate the effects of the wave strength on the particle orientations, we considered only data from particles after they had evolved in the wave field for more than 10 wave periods; we found empirically that after this amount of time had elapsed, particle statistics were stationary in time. To additionally remove any residual effects of wave-driven oscillations and the phase dependence they may introduce, we also averaged the data over wave periods so that we could study the mean particle orientations as opposed to the transient wobble.

In Fig. 9 we plot PDFs of ϕ for these data for negatively buoyant large disks and long rods at different depths in the water column. As quantified by the depth-dependent wave shear $ka(z)$ defined
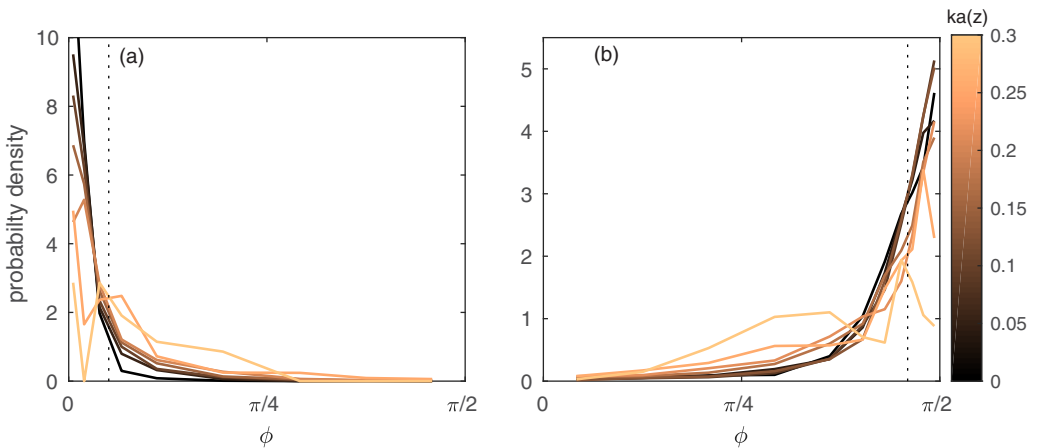

FIG. 9. PDFs of the polar angle ϕ for (a) large disks ($\beta = 1.005$) and (b) long rods ($\beta = 1.01$) for different values of the nondimensional wave shear $ka(z)$, as indicated by the shading. The dotted lines show the theoretical wave-preferred angle ϕ_w^*. The preferred settling angle is $\phi_s^* = 0$ for the disks and $\phi_s^* = \pi/2$ for the rods. Data are combined from all three wave cases, but only for particles that had evolved in the waves for at least 10 wave periods.
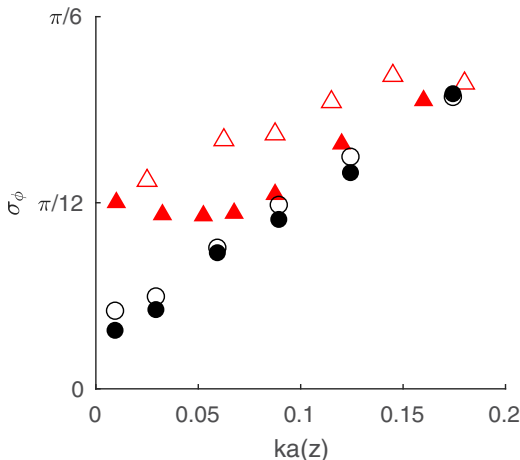
FIG. 10. Standard deviation of the wave-period-averaged polar angle ϕ as a function of nondimensional wave shear $ka(z)$ for different particle shapes: long rods (closed triangles), short rods (open triangles), large disks (closed circles), and small disks (open circles). The data come from $\beta = 1.005$ for all shapes except long rods which have $\beta = 1.01$, and data are included only for particles that had evolved in the waves for at least 10 wave periods.

above, particles lower in the water column feel the effects of the waves less strongly. For large $ka(z)$, both disks and rods show a strong tendency to be oriented at the wave-preferred angle ϕ_w^*. But as $ka(z)$ decreases, the peak in the PDFs moves toward the settling-preferred angle ϕ_s^*. This behavior supports our interpretation that the particle orientation is controlled by a competition between wave motion and settling.

However, even though the PDFs show peaks at ϕ_w^* and ϕ_s^*, they are not δ functions: we always observe spread in the PDFs. To quantify this spread and quantify how it depends on the wave strength, we plot σ_ϕ for all particle shapes as a function of $ka(z)$ in Fig. 10. For all particle shapes, we observe an overall increase of σ_ϕ with $ka(z)$, meaning that as the effective strength of the waves grows, so does the variability in the particle orientation. In Fig. 10 there is a slight difference in the relationship between the angle standard deviation and the nondimensional wave shear for the long rods. However, they are heavier than the rest of the particles, which we expect to be the cause of this difference seen in the data. Thus, while waves can focus particle orientations over time, the competition between waves and settling—and therefore the existence of two preferred orientations, ϕ_w^* and ϕ_s^*—means that the presence of waves can also have a scrambling effect on particle orientation.

C. Out-of-plane orientations

We have previously shown theoretically that there are fixed points in the dynamics of noninertial, infinitesimal spheroids for both $\theta = 0$ and $\theta = \pi/2$; that is, for spheroids that lie in the plane of the wave motion and orthogonal to it [7]. In the noninertial case, the $\theta = \pi/2$ case is unstable, and so the particles will naturally orient themselves to lie in the plane of the waves. However, when inertia is introduced (as it is in these experiments), the stability of these orientations may change.

The out-of-plane orientation of spheroids is known in the literature on particles in shear flows as log rolling, in part because particles are observed to rotate about their symmetry axis which, in this orientation, is aligned with the vorticity axis. Shear flows are, however, rotational, whereas surface gravity waves are not; thus, we may expect to see different behavior here. To check for log rolling, we marked our disks with a cross that could be seen in our images. However, unlike in the shear
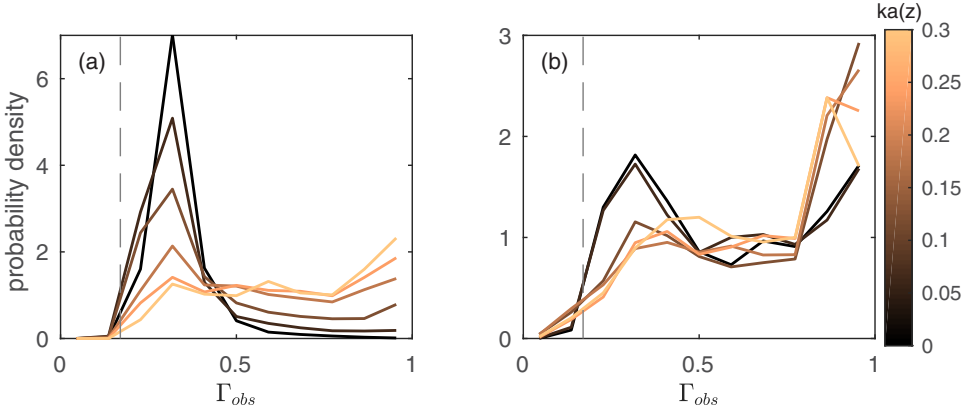
FIG. 11. PDFs of the apparent aspect ratio Γ_{obs} of large disks with (a) $\beta = 1.005$ and (b) $\beta = 1$ for different values of the nondimensional wave shear $ka(z)$, as indicated by the shading. Data are combined from all three waves cases over the entire experimental record. The dashed line indicates the actual aspect ratio of the particles.

flow case, we did not observe evidence of log rolling: over the course of the experiments, only a small drift in the orientation of the cross was observed on timescales much longer than the wave period.

Just because the particles did not rotate about their symmetry axis, however, does not mean that they did not sometimes orient orthogonal to the plane of the waves. To quantify this effect, we measured the apparent particle aspect ratio Γ_{obs} as observed in the images. $\Gamma_{\mathrm{obs}} = 1$ corresponds to a particle aligned orthogonal to the wave plane, since both the rods and disks had circular cross sections. Γ_{obs} values closer to the actual aspect ratio of the particle Γ, however, mean that the particle is aligned in the plane of the waves.

We show PDFs of Γ_{obs} for large disks in Fig. 11 and for small disks in Fig. 12. In both cases, we include data for both negatively buoyant and neutrally buoyant particles, as well as for particles with different values of the wave shear $ka(z)$. Neutrally buoyant disks have a strong tendency to
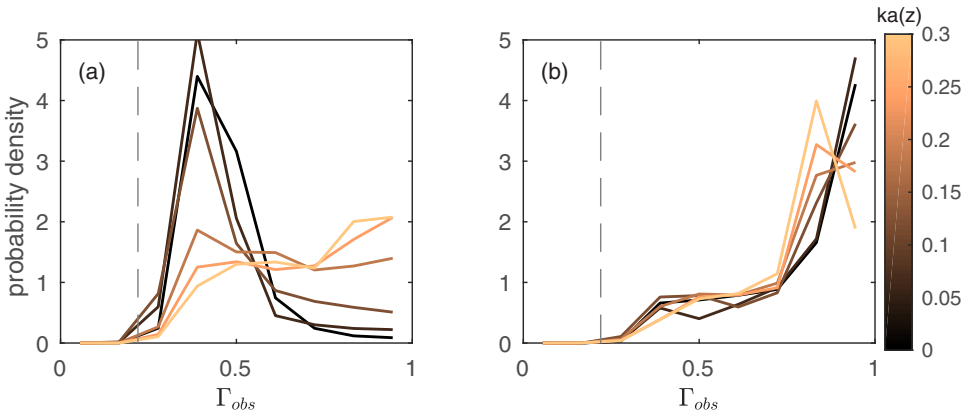

FIG. 12. PDFs of the apparent aspect ratio Γ_{obs} of small disks with (a) $\beta = 1.005$ and (b) $\beta = 1$ for different values of the nondimensional wave shear $ka(z)$, as indicated by the shading. Data are combined from all three waves cases over the entire experimental record. The dashed line indicates the actual aspect ratio of the particles.

align orthogonal to the wave plane for all values of $ka(z)$. There is more variation with the wave strength for negatively buoyant disks; both large and small negatively buoyant disks are more likely to orient out of plane for higher values of $ka(z)$. These results suggest that waves stabilize the out-of-plane orientation for these particles, and that settling destabilizes it. It appears that it is the finite size of the particles that leads to this effect, since in the neutrally buoyant case, finite size is the only difference between the experimental conditions and the theory that predicts that this position is unstable. Finally, we note that while we show data here only for disks, we also observed examples of rods oriented out of plane. However, as they are more difficult to measure in this orientation due to their small cross-sectional area, our data for out-of-plane rods are quite noisy.

We also observe that transitions occur in the data in Figs. 11(a) and 11(b) and Fig. 12(a) between particles aligned out of plane and in the plane of the waves. As we described in Sec. III D, we can interpret $ka(z)$ to form a shear particle Reynolds number Re_s which can then be related to similar transitions to log rolling seen in oblate particles in shear flow. The majority of particles are in the log-rolling orientation in our experiments for $\mathrm{Re}_s \geqslant 30$ for neutrally buoyant large disks, $\mathrm{Re}_s \geqslant 100$ for negatively buoyant large disks, and $\mathrm{Re}_s \geqslant 45$ for negatively buoyant small disks. It should be noted that these values of Re_s are not directly comparable to values in the shear flow literature because in this case the particles feel an oscillating shear flow. However, the overall trends agree with the work of Rosén *et al.* [17] who found that small oblate particles were stabilized in their log-rolling mode in steady shear flow with intermediate Re_s values, and that the effect of both small particle and fluid inertia acted to stabilize the log-rolling mode.

These data show that waves can stabilize negatively buoyant, settling disks in the log-rolling orientation. The log-rolling orientation presents the particle's minimum surface area in the vertical direction. In the absence of flow, these particles tend to maximize their vertical drag, but the waves can instead orient them such that their vertical drag is minimized. This is an important result in the context of predicting *in situ* settling velocities of particles in the ocean.

V. CONCLUSIONS

Our experimental findings both confirm and expand on our previous theoretical results for the behavior of noninertial particles under surface gravity waves. We find that finite-sized particles that are nearly neutrally buoyant tend to adopt either their wave-preferred angle or their settling-preferred angle; which of these angles dominates the dynamics is controlled by the wave strength and the particle density. We also find, though, that increased wave strength leads to a larger angular spread about this preferential orientation. Finally, we show that waves can stabilize out-of-plane orientations for finite-sized disks, contrary to theoretical results for noninertial spheroids. However, this orientation is destabilized by settling.

Our results have potentially significant results for predicting the transport of nonspherical particles in wave-dominated flows, such as those in the upper ocean, since particle orientation is coupled to translation through drag and lift forces. Accurately accounting for the dynamical biases we have found in the particle orientations is therefore essential for predicting the residence time of a particle in the water column and thus the horizontal distance it can be transported. We anticipate that these effects will have important ramifications for the future modeling of, for example, the dispersion of marine microplastics.

[1] L. G. Leal, Particle motions in a viscous fluid, Annu. Rev. Fluid Mech. **12**, 435 (1980).

[2] T. Rosén, J. Einarsson, A. Nordmark, C. K. Aidun, F. Lundell, and B. Mehlig, Numerical analysis of the angular motion of a neutrally buoyant spheroid in shear flow at small Reynolds numbers, Phys. Rev. E **92**, 063022 (2015).

[3] Y. Cui, J. Ravnik, M. Hriberšek, and P. Steinmann, A novel model for the lift force acting on a prolate spheroidal particle in an arbitrary non-uniform flow. Part I. Lift force due to the streamwise flow shear, Int. J. Multiph. Flow **104**, 103 (2018).

[4] G. A. Voth and A. Soldati, Anisotropic particles in turbulence, Annu. Rev. Fluid Mech. **49**, 249 (2017).

[5] N. Khurana and N. T. Ouellette, Interactions between active particles and dynamical structures in chaotic flow, Phys. Fluids **24**, 091902 (2012).

[6] G. De Carolis, P. Olla, and L. Pignagnoli, Effective viscosity of grease ice in linearized gravity waves, J. Fluid Mech. **535**, 369 (2005).

[7] M. H. DiBenedetto and N. T. Ouellette, Preferential orientation of spheroidal particles in wavy flow, J. Fluid Mech. **856**, 850 (2018).

[8] M. H. DiBenedetto, N. T. Ouellette, and J. R. Koseff, Transport of anisotropic particles under waves, J. Fluid Mech. **837**, 320 (2018).

[9] L. P. Wang and M. R. Maxey, Settling velocity and concentration distribution of heavy particles in homogeneous isotropic turbulence, J. Fluid Mech. **256**, 27 (1993).

[10] M. R. Maxey, The gravitational settling of aerosol particles in homogenous turbulence and random flow fields, J. Fluid Mech. **174**, 441 (1987).

[11] P. Nielsen, Turbulence effects on the settling of suspended particles, J. Sediment. Res. **63**, 835 (1993).

[12] K. Gustavsson, J. Jucha, A. Naso, E. Lévêque, A. Pumir, and B. Mehlig, Statistical Model for the Orientation of Non-Spherical Particles Settling in Turbulence, Phys. Rev. Lett. **119**, 254501 (2017).

[13] C. Siewert, R. P. J. Kunnen, M. Meinke, and W. Schröder, Orientation statistics and settling velocity of ellipsoids in decaying turbulence, Atmospheric Res. **142**, 45 (2014).

[14] G. B. Jeffery, The motion of ellipsoidal particles immersed in a viscous fluid, Proc. R. Soc. Lond. A **102**, 161 (1922).

[15] N. R. Challabotla, L. Zhao, and H. I. Andersson, Orientation and rotation of inertial disk particles in wall turbulence, J. Fluid Mech. **766**, R2 (2015).

[16] J. Einarsson, F. Candelier, F. Lundell, J. R. Angilella, and B. Mehlig, Rotation of a spheroid in a simple shear at small Reynolds number, Phys. Fluids **27**, 063301 (2015).

[17] T. Rosén, M. Do-Quang, C. K. Aidun, and F. Lundell, Effect of fluid and particle inertia on the rotation of an oblate spheroidal particle suspended in linear shear flow, Phys. Rev. E **91**, 053017 (2015).

[18] M. Shin and D. L. Koch, Rotational and translational dispersion of fibres in isotropic turbulent flows, J. Fluid Mech. **540**, 143 (2005).

[19] H. I. Andersson and A. Soldati, Anisotropic particles in turbulence: Status and outlook, Acta Mech. **224**, 2219 (2013).

[20] A. D. Bordoloi and E. Variano, Rotational kinematics of large cylindrical particles in turbulence, J. Fluid Mech. **815**, 199 (2017).

[21] S. Parsa and G. A. Voth, Inertial Range Scaling in Rotations of Long Rods in Turbulence, Phys. Rev. Lett. **112**, 024501 (2014).

[22] W. E. Dietrich, Settling velocity of natural particles, Water Resour. Res. **18**, 1615 (1982).

[23] S. Tran-Cong, M. Gay, and E. E. Michaelides, Drag coefficients of irregularly shaped particles, Powder Technol. **139**, 21 (2004).

[24] L. Khatmullina and I. Isachenko, Settling velocity of microplastic particles of regular shapes, Marine Poll. Bull. **114**, 871 (2016).

[25] A. Hazzab, A. Terfous, and A. Ghenaim, Measurement and modeling of the settling velocity of isometric particles, Powder Technol. **184**, 105 (2008).

[26] Q. Zhou and N. S. Cheng, Experimental investigation of single particle settling in turbulence generated by oscillating grid, Chem. Eng. J. **149**, 289 (2009).

[27] D. Lopez and E. Guazzelli, Inertial effects on fibers settling in a vortical flow, Phys. Rev. Fluids **2**, 24306 (2017).

[28] S. Bounoua, G. Bouchet, and G. Verhille, Tumbling of Inertial Fibers in Turbulence, Phys. Rev. Lett. **121**, 124502 (2018).

[29] H. A. Becker, The effects of shape and Reynolds number on drag in the motion of a freely oriented body in an infinite fluid, Can. J. Chem. Eng. **37**, 85 (1959).

[30] E. K. Marchildon, A. Clamen, and W. H. Gauvin, Drag and oscillatory motion of freely falling cylindrical particles, Can. J. Chem. Eng. **42**, 178 (1964).

[31] J. Einarsson, J. R. Angilella, and B. Mehlig, Orientational dynamics of weakly inertial axisymmetric particles in steady viscous flows, Physica D **278**, 79 (2014).

[32] Z. Yu, N. Phan-Thien, and R. I. Tanner, Rotation of a spheroid in a Couette flow at moderate Reynolds numbers, Phys. Rev. E **76**, 026310 (2007).

[33] W. Mao and A. Alexeev, Motion of spheroid particles in shear flow with inertia, J. Fluid Mech. **749**, 145 (2014).

[34] S. Wang, Plunger-type wavemakers: Theory and experiment, J. Hydraul. Res. **12**, 357 (1974).

[35] B. C. Cole, G. G. Marcus, S. Parsa, S. Kramel, R. Ni, and G. A. Voth, Methods for measuring the orientation and rotation rate of 3D-printed particles in turbulence, J. Vis. Exp. **112**, e53599 (2016).

[36] N. T. Ouellette, H. Xu, and E. Bodenschatz, A quantitative study of three-dimensional Lagrangian particle tracking algorithms, Exp. Fluids **40**, 301 (2006).

[37] D. H. Kelley and N. T. Ouellette, Using particle tracking to measure flow instabilities in an undergraduate laboratory experiment, Am. J. Phys. **79**, 267 (2011).

[38] S. A. Hughes, Laboratory wave reflection analysis using co-located gages, Coast. Eng. J. **20**, 223 (1993).

[39] M. S. Longuet-Higgins, Mass transport in water waves, Philos. Trans. Royal Soc. A **245**, 535 (1953).